American Mineralogist, Volume 83, pages 1209–1219, 1998

Formation of secondary minerals and its effect on anorthite dissolution

Takashi Murakami,[1,*] Toshihiro Kogure,[1] Hiroyuki Kadohara,[1] and Toshihiko Ohnuki[2]

[1]Mineralogical Institute, University of Tokyo, Bunkyo-ku, Tokyo 113, Japan
[2]Environmental Geochemistry Laboratory, Japan Atomic Energy Research Institute, Tokai, Ibaraki 319-11, Japan

Abstract

To examine the relationship between product secondary minerals and dissolution of anorthite ($An_{95}Ab_5$ from Fugoppe, Hokkaido, Japan), anorthite batch dissolution experiments were carried out. The dissolution experiments were done at 90, 150, and 210 °C for 3 to 355 days at pH 4.56 measured at 25 °C, which corresponds to 4.69, 4.97, and 5.40 at the respective experimental temperatures. A sequence of secondary minerals including boehmite, ''modified boehmite,'' and kaolinite formed with increasing time. Modified boehmite, probably a metastable phase, is basically similar to boehmite in structure, but their stacking orders of the Al octahedral layers as well as morphologies and chemistries are different. Modified boehmite shows laminations normal to the b^* axis and contains 3 to 30 mol% Si. Silicon may be present between the Al octahedral layers of modified boehmite. The anorthite dissolution is incongruent under the above conditions and approximated by a two-stage process. The first is characterized by the formation of boehmite, and the second by formation of modified boehmite. The dissolution rate in the second stage is slower than the first by approximately one order of magnitude because of the saturation state with respect to anorthite. To estimate the effect of the formation of secondary minerals on the anorthite dissolution, Gibbs free energies of anorthite dissolution (ΔG) were calculated, assuming conditions without the formation of secondary minerals. The calculations reveal that the formation of secondary minerals decreases the ΔG values significantly, and thus we can predict that the dissolution rates of anorthite increase due to the influence of the secondary minerals on ΔG. Modified boehmite functions as a sink for Si, and thus accelerates the dissolution rate of anorthite. The results indicate that the overall dissolution rate near equilibrium is affected by both the saturation with respect to a primary mineral and the formation of secondary minerals, but in the opposite sense.

Introduction

Feldspar dissolution has been studied extensively [see reviews by Blum (1994) and Blum and Stillings (1995)], mainly because feldspar is the most abundant mineral in the exposed crust (Blatt and Jones 1975) and it thus plays an important role in element transport and cycles at the Earth's surface. For instance, dissolution of feldspars, especially anorthite, affects the concentration of atmospheric CO_2 (Berner et al. 1983; Berner and Barron 1984; Brady 1991; Berner 1992; Brady and Caroll 1994; Lasaga et al. 1994; Berner 1995), and thus the temperature at the Earth's surface.

The early stage of silicate dissolution has been documented by controlled laboratory experiments where the solution compositions are maintained ''far from equilibrium'' with the solid (flow-type experiments) to avoid precipitation of secondary minerals (e.g., White and Brantley 1995). The approach of using surface-coordination complexes has successfully explained the initial dissolution step: The dissolution rate of feldspar was shown to be a function of the concentrations of H^+ and OH^- and, thus, surface reactions involving H^+ and OH^- control the dissolution (Blum and Stillings 1995). However, the dissolution rates measured in the laboratory are larger than those in the field by a few orders of magnitude, which is probably caused by several factors including: (1) temperature differences; (2) differences in mineral-surface conditions; (3) the presence of higher Fe and Al concentrations in natural systems; (4) a saturation-state difference; and (5) a much lower surface area for minerals actually in contact with water in natural systems (Blum 1994). Of these causes, the last two are likely to be the most important.

Velbel (1993) compared the dissolution rate ratios of different minerals in laboratory experiments to those in nature and concluded that the difference in dissolution rates is caused by physical controls in nature such as heterogeneous water flow, which results in a decrease in effective surface area of minerals. Several other workers have reached a similar conclusion, arguing that the ob-

* E-mail: murakami@min.s.u-tokyo.ac.jp

0003–004X/98/1112–1209$05.00

TABLE 1. The composition and chemical formula of starting anorthite

Oxide	SiO_2	Al_2O_3	FeO*	CaO	MgO	MnO	Na_2O	K_2O	Total
wt%	44.15(42)	34.98(29)	0.49(4)	18.98(15)	0.10(1)	0.01(1)	0.51(2)	0.02(1)	99.23
Cations per 8 oxygen atoms	2.06	1.92	0.02	0.95	0.01	0.00	0.05	0.00	5.01

Note: Values in parentheses represent standard deviations, referring to the last decimal place.
* All Fe as FeO.

served difference in dissolution rates is due to the overestimation of the reactive surface area of natural minerals (Schnoor 1990; Velbel 1990; Rowe and Brantley 1993; Swoboda-Colberg and Drever 1993). On the other hand, it is often observed in naturally weathered samples that secondary minerals grow in intimate contact with the primary, dissolving minerals when the weathering process occurs at very low fluid/mineral ratios (e.g., Casey et al. 1993a). The fact that different primary minerals weather to specific phases, for instance, biotite to vermiculite and plagioclase to kaolinite in granite weathering (Velde and Meunier 1987), suggests that the solutions in contact with primary minerals are close to equilibrium with respect to the secondary minerals and that local reactions occur. Laboratory results indicate that a saturation state effect could be another explanation for the discrepancy with dissolution rates observed in nature (Amrhein and Suarez 1992; Burch et al. 1993). Consequently, dissolution near equilibrium with the primary minerals may be important to understand natural weathering.

Less attention has been paid to the comparison of natural weathering to laboratory dissolution in the presence of secondary phases (Hochella and Banfield 1995; Nagy 1995). Recent experiments on sanidine and albite dissolution have shown that secondary minerals control the dissolution of the primary mineral (Alekseyev et al. 1997). Although the precipitation of secondary minerals and subsequent change in chemical affinity can make it difficult to interpret dissolution data (Hellmann 1994), the reaction processes in nature cannot be elucidated precisely without understanding both the solution evolution and the mineral paragenesis. In addition, laboratory experiments must reproduce many textures observed in nature (Casey et al. 1993a; Casey et al. 1993b). To address some of these problems, we carried out dissolution experiments on anorthite under conditions where secondary minerals coexist with anorthite to examine how dissolution is affected by the presence of secondary minerals. Anorthite was chosen because its dissolution rate is the fastest among feldspars and because its high Ca content has an important effect on the carbon cycle in nature.

EXPERIMENTAL METHODS

Starting material

Specimens used for the dissolution experiments were single crystals of anorthite from Fugoppe, Hokkaido, Japan. The original crystals of anorthite in Fugoppe are as big as 1.5–3 cm in size, and occur in tuffs in pyroxene andesites (Harada and Hariya 1984). The original surfaces of the crystals already had etch pits. The original crystals were broken, and smaller pieces with fresh surfaces were used for the dissolution experiments. The composition of the anorthite specimen was determined by electron microprobe analysis (EMPA, JEOL JXA-733) at an operating voltage of 15 kV and a beam current of 5 nA. Data reduction followed the scheme of Benece and Albee (1968). The following standards were used: Na = albite; K = adularia; Ca = wollastonite; and Si, Al, Fe, Mg, and Mn = oxides. The average value of 20 measurements on the starting sample as well as the resultant mineral formula are given in Table 1.

Dissolution experiments

The single crystals of anorthite, roughly 1 mm × 1 mm × 1 mm in size with six, approximately rectangular faces were prepared by crushing. The surface areas of the single crystals were measured geometrically under a light microscope (Table 2). The single crystals were washed ultrasonically in acetone to remove fine particles from the surface. The surface of one of the single crystals was examined by scanning electron microscopy (SEM), to confirm that there were few fine particles on the surface. Distilled and deionized water with a buffer of sodium acetate (0.03 mol/L) and acetate was used as a reactant solution and pH was adjusted to 4.56 by acetate at room temperature. Acetate is often used as a pH buffer (e.g., Franklin et al. 1994), and has no significant effect on feldspar dissolution (Welch and Ullman 1993). The ionic strength of the reactant solution was 0.067. Four to five single crystals of anorthite with a total surface area of approximately 0.3 cm^2 were put in a Teflon vessel with a reactant solution of approximately 9 mL; the ratio of surface area to solution (cm^2/mL) was adjusted to 1:30. The Teflon vessel was then placed in an electric oven. The run temperatures were 90, 150, and 210 °C (±2.5 °C), and the run durations were 3 to 355 days. After the dissolution experiments, the vessel was cooled to room temperature in 30 min, and the pH of the solution was measured at room temperature. The solution was then separated from the solids by 0.22 μm filter, and a solution with 10 wt% nitric acid was added so that the final solution contained 1 wt% nitric acid to lower the pH and preserve the metals for analysis. The solids were washed gently in acetone and dried.

Analytical techniques

The morphology of the solid samples was examined by SEM (Hitachi S4500) at an operating voltage of 15 kV.

TABLE 2. Solution data for anorthite dissolution

T (°C)	Duration (days)	Si (mol/L)	Ca (mol/L)	Al (mol/L)	Si (mol/m²)	Ca (mol/m²)	SA* (m²)	pH† Before	pH† After
90	3	1.40(<1) × 10⁻⁵‡	6.57(6) × 10⁻⁶	9.67(7) × 10⁻⁶	4.20(<1) × 10⁻³	1.97(2) × 10⁻³	3.23 × 10⁻⁵	4.56(4.69)	4.58(4.71)
90	10	6.36(1) × 10⁻⁵	2.97(5) × 10⁻⁶	1.13(<1) × 10⁻⁴	1.93(<1) × 10⁻²	9.04(1) × 10⁻³	3.07 × 10⁻⁵	4.56(4.69)	4.50(4.63)
90	30	2.36(<1) × 10⁻⁴	1.04(<1) × 10⁻⁴	1.29(<1) × 10⁻⁴	7.12(3) × 10⁻²	3.15(1) × 10⁻²	3.08 × 10⁻⁵	4.56(4.69)	4.54(4.67)
90	90	5.57(<1) × 10⁻⁴	2.73(<1) × 10⁻⁴	4.21(5) × 10⁻⁶	1.64(<1) × 10⁻¹	8.02(1) × 10⁻²	3.10 × 10⁻⁵	4.56(4.69)	4.52(4.65)
90	159	6.09(1) × 10⁻⁴	3.12(1) × 10⁻⁴	3.08(<1) × 10⁻⁵	1.75(<1) × 10⁻¹	8.95(4) × 10⁻²	2.95 × 10⁻⁵	4.56(4.69)	4.56(4.69)
90	355	8.14(<1) × 10⁻⁴	4.28(<1) × 10⁻⁴	1.64(1) × 10⁻⁵	2.16(<1) × 10⁻¹	1.14(<1) × 10⁻¹	2.98 × 10⁻⁵	4.56(4.69)	4.59(4.72)
150	3	2.76(2) × 10⁻⁴	1.24(6) × 10⁻⁴	2.39(7) × 10⁻⁶	8.11(6) × 10⁻²	3.65(2) × 10⁻²	3.20 × 10⁻⁵	4.56(4.97)	4.58(4.99)
150	10	7.72(2) × 10⁻⁴	3.79(2) × 10⁻⁴	1.04(<1) × 10⁻⁴	2.30(<1) × 10⁻¹	1.13(<1) × 10⁻¹	3.00 × 10⁻⁵	4.56(4.97)	4.53(4.94)
150	30	1.27(<1) × 10⁻³	6.25(1) × 10⁻⁴	1.37(<1) × 10⁻⁴	3.51(1) × 10⁻¹	1.73(<1) × 10⁻¹	3.07 × 10⁻⁵	4.56(4.97)	4.54(4.95)
150	90	1.96(<1) × 10⁻³	9.77(2) × 10⁻⁴	1.10(3) × 10⁻⁵	4.83(<1) × 10⁻¹	2.41(<1) × 10⁻¹	3.10 × 10⁻⁵	4.56(4.97)	4.60(5.01)
210	3	9.09(7) × 10⁻⁴	4.35(4) × 10⁻⁴	8.77(7) × 10⁻⁶	2.67(2) × 10⁻¹	1.28(1) × 10⁻¹	3.20 × 10⁻⁵	4.56(5.40)	4.56(5.40)
210	10	1.64(<1) × 10⁻³	7.75(2) × 10⁻⁴	2.52(1) × 10⁻⁵	4.79(1) × 10⁻¹	2.26(<1) × 10⁻¹	3.23 × 10⁻⁵	4.56(5.40)	4.56(5.40)
210	34	1.98(<1) × 10⁻³	9.75(1) × 10⁻⁴	2.99(2) × 10⁻⁵	5.40(1) × 10⁻¹	2.66(<1) × 10⁻¹	3.17 × 10⁻⁵	4.56(5.40)	4.62(5.46)
210	97	2.66(<1) × 10⁻³	1.39(<1) × 10⁻³	2.20(2) × 10⁻⁵	6.35(2) × 10⁻¹	3.32(<1) × 10⁻¹	3.19 × 10⁻⁵	4.56(5.40)	4.63(5.47)
210	165	3.28(<1) × 10⁻³	1.82(<1) × 10⁻³	2.31(2) × 10⁻⁵	6.41(1) × 10⁻¹	3.56(1) × 10⁻¹	3.26 × 10⁻⁵	4.56(5.40)	4.74(5.58)

* SA stands for surface area.
† Values of pH measured at 25 °C, and in parentheses, those at experimental temperatures calculated from respective measured pH values.
‡ Parenthesis shows standard deviation of the measurement.

The secondary minerals formed by the anorthite dissolution were subjected to X-ray diffraction analysis (XRD) (Rigaku RINT 2000), and their compositions determined qualitatively by SEM equipped with an energy dispersive X-ray analyzer (EDX) (JEOL JSM-5400) at an operating voltage of 20 kV. The secondary minerals were examined further by high-resolution transmission electron microscopy (HRTEM) and analytical electron microscopy (AEM). TEM samples were prepared by one of two methods: Either the solid samples were gently crushed and ground, dispersed in ethanol, and placed on TEM grids or the solid samples were impregnated in epoxy resin and cut by ultramicrotomy. A JEOL JEM-2010 and a Hitachi HF 2000 were used for the HRTEM and AEM studies.

Silicon, Al, and Ca concentrations in a solution after dissolution were measured three times for each run by inductively coupled plasma (ICP) atomic emission spectrometry (Seiko SPS7700). The solution analyses are summarized in Table 2.

To examine the effect of saturation state on the dissolution rate of anorthite, we calculated a value of log (*Q*/*K*) for each run at the experimental temperature using the computer code EQ3NR (Wolery 1992), where *Q* is the activity product of species and *K* is the equilibrium constant of anorthite. The pH values at the experimental temperatures were also calculated based on the measured pH values at room temperature, considering the pH values of the acetate buffer at the experimental temperatures (Table 2). Input solution data are from Table 2. Activities of the solution species were calculated using the Davies equation. The thermodynamic database in EQ3NR was used in the calculations.

RESULTS

Etch pits ~5 μm in diameter that were already present on the surface of the starting anorthite became larger (e.g., about 15 μm in diameter after 97 day dissolution at 210 °C) with dissolution. At 210 °C for 3 days, the anorthite surface was partly covered with boehmite (Fig. 1a), which was identified by selected area electron diffraction (SAED) and EDX. Two porous layers of boehmite grains were developed on the anorthite surface; one composed of ~2 μm diameter particles developed adjacent to the surface and the other consisting of ~1 μm diameter particles developed in contact with the solution. The two layer structure is illustrated in Figure 1b. The anorthite surfaces were not fully covered with the secondary minerals, and only part of each grain was in contact with the surfaces. Consequently, the two-layer structure did not affect the anorthite dissolution by inhibition of diffusion. After 10 to 165 days at 210 °C, the two-layer structure was maintained (Figs. 1b and 1d). The morphology of product grains after the 10 day run was similar to that of the 3 day run. However, the surfaces roughly parallel to [010] of the boehmite-like grains were not smooth (arrows in Fig. 1c), and with time, the product grains showed a laminated morphology (Fig. 1d). AEM showed that the laminated grains contain variable amounts of Si in addition to Al; the Si/Al molar ratio ranged from 1/30 to 10/30 (Fig. 2). The phase containing Si is hereafter referred to as modified boehmite and described in detail below. After the 97 day run, kaolinite, confirmed by TEM and AEM, was formed as well as modified boehmite. The sequence from boehmite to modified boehmite was also observed for the 90 and 150 °C experiments, although the formation of kaolinite was not found even in the longest duration experiments in the present study. We did not find any structural inheritance (i.e., topotaxy) between anorthite and the secondary minerals such as found, for instance, in olivine (Banfield et al. 1990) and pyroxene (Banfield et al. 1991). This result is expected because of the absence of any structural similarity between anorthite and the secondary minerals (e.g., Banfield and Eggleton 1990). Figure 3 summarizes the paragenesis of secondary minerals, and indicates that boehmite does not coexist with modified boehmite.

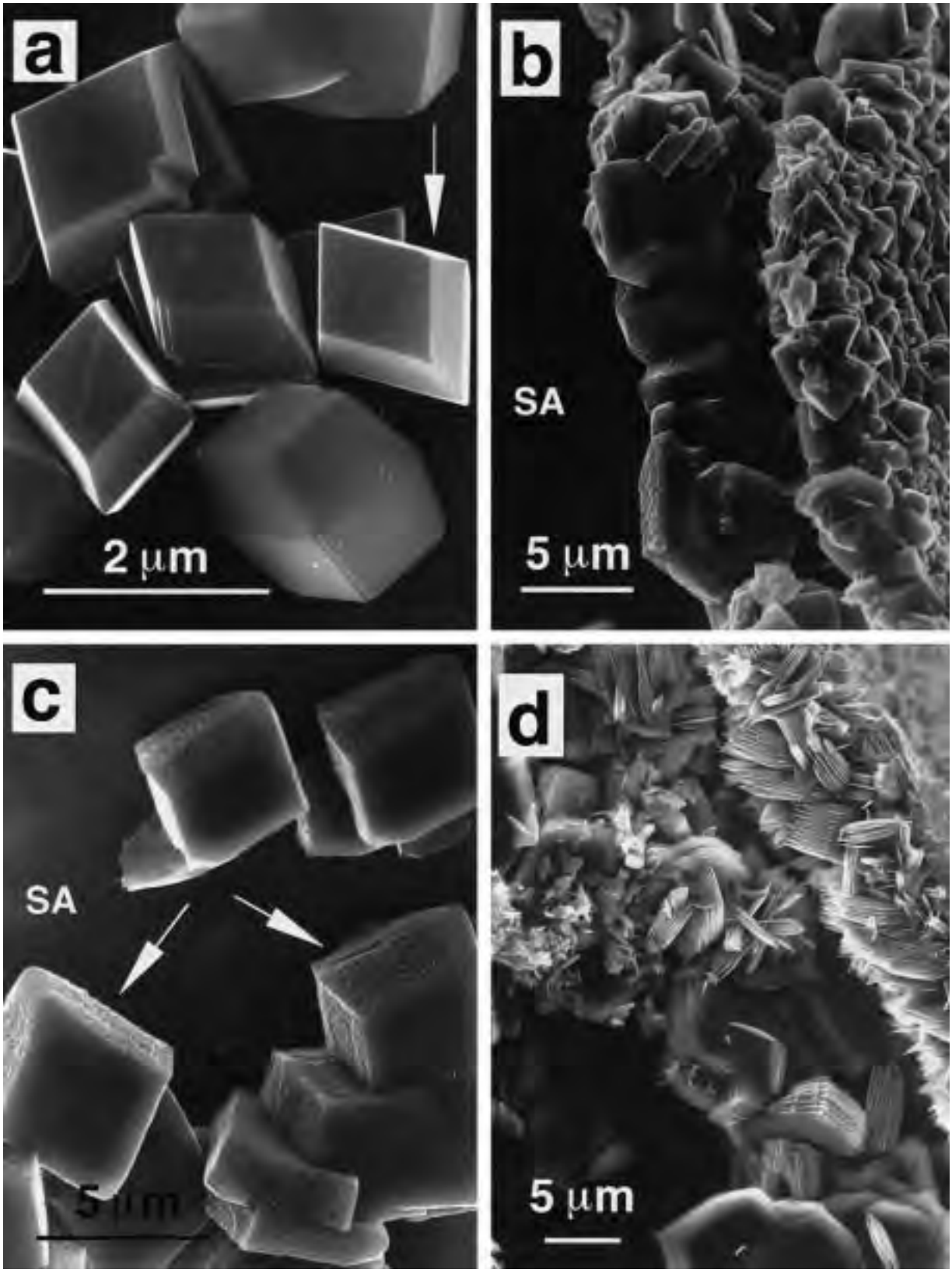
a
2 μm
b
SA
5 μm
c
SA
5 μm
d
5 μm

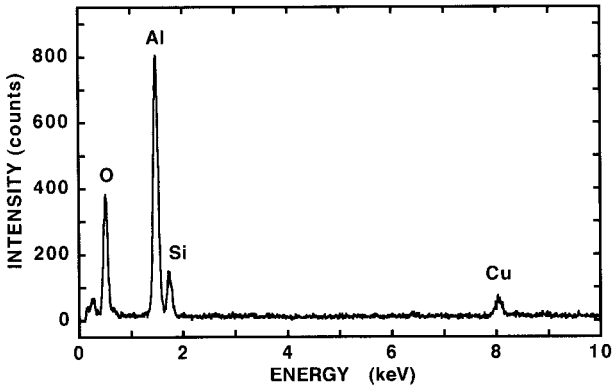

FIGURE 2. Analytical electron microscope EDX profile of typical modified boehmite formed after 97 days dissolution at 210 °C. The Cu peak arises from the grid that holds the sample.

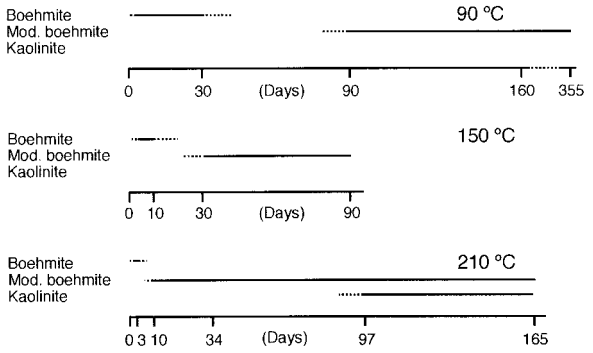

FIGURE 3. Schematic diagram showing the paragenesis of secondary minerals. The solid lines represent the presence of the secondary minerals confirmed by observation and the dotted lines their possible existence.

The powder XRD pattern of modified boehmite was almost the same as that of boehmite [Amam, a = 0.36936, b = 1.2214, and c = 0.28679 nm, e.g., Christoph et al. (1979); see Fig. 4]. The [010] SAED pattern of modified boehmite was also the same as that of boehmite (Figs. 5a and 5b, respectively). Both boehmite and modified boehmite transformed in the (010) plane to γ-Al_2O_3 [spinel structure (Fd3m), Rooksby (1961)] by electron irradiation (Fig. 5c). However, in addition to the difference in chemistry, a difference was observed between the structure of boehmite and modified boehmite along the b* axis. Figure 6a shows part of a laminated structure, normal to the b* axis, at the rim of modified bohemite grains, such as those shown in Figure 1d. The diffraction spots of modified boehmite are elongated normal and parallel to the b* axis (Fig. 6b) because of the micromorphology (Fig. 6a) and irregular stacking (Figs. 7b and 7c), respectively. The modified boehmite is beam sensitive and the SAED pattern changes progressively to that shown in Figure 6c due to the beam damage. HRTEM imaging of finer-grained modified boehmite (a few micrometers in size) shows lattice fringes along the b* axis very similar to those of boehmite, i.e., repeat of black and white contrast of a 0.61 nm periodicity (Fig. 7a). Thus, the Al octahedral layers of boehmite are retained in modified boehmite. Discontinuities and edge dislocations are present in the finer-grained modified boehmite (arrows in Fig. 7a). However, another finer-grained, modified boehmite crystal also retains a ~0.61 nm periodicity, but exhibits irregular contrast along the b* axis (Fig. 7b). This crystal did not have a long-range periodicity compared to that in Figure 7a. Figure 7c shows (010) lattice fringes at the tip of coarser-grained modified boehmite (see Fig. 6a), in which a further decrease in the long-range periodicity is observed, and the crystal was divided into packets 3–7 nm thick.

AEM data show that, in general, the coarser grains of modified boehmite in the layer adjacent to the surface (Fig. 1b) contain more Si than the finer grains in the layer adjacent to the solution. More importantly, SEM-EDX analysis shows that 3 mol% Si is present at the center of a grain (e.g., see Fig. 1d) when the electron beam was roughly parallel to the b* axis. On the other hand, the rim of a grain contains ~15 mol% Si with the electron beam normal to the b* axis (e.g., see Fig. 6a).

Figures 8a, 8b, and 8c show the variation in dissolved cation concentration with time for the 90, 150, and 210 °C experiments, respectively. Silicon and Ca were dissolved in solution roughly, but not exactly, in accordance with the stoichiometry of anorthite (Table 1). On the other hand, most Al precipitated, after it was released, as boehmite or modified boehmite. The Si release variation with time indicates that anorthite dissolution is approximated by a two-stage process: The first stage has a higher dissolution rate than the second, and the Si concentration increases linearly in each stage as a function of time (Figs. 8a, 8b, and 8c). The comparison of the paragenesis of secondary minerals (Fig. 3) with the variation in Si concentration reveals the first stage corresponds to the presence of boehmite and the second one to that of modified boehmite.

←

FIGURE 1. SEM images of (**a**) boehmite crystals on the surface of anorthite after 3 days dissolution at 210 °C. (**b**) Modified boehmite on the surface of anorthite (labeled with SA) after 10 days dissolution at 210 °C. (**c**) Modified boehmite crystals with rough surface parallel to [010] on the surface of anorthite (labeled with SA) after 10 days dissolution at 210 °C. (**d**) Modified boehmite crystals with laminated morphology on the surface of anorthite after 97 days dissolution at 210 °C. A two-layer structure on the anorthite surface is observed throughout the experiments. The rough surface of modified boehmite (arrows in Fig. 1c) is distinct from the smooth surface of boehmite (arrow in Fig. 1a).

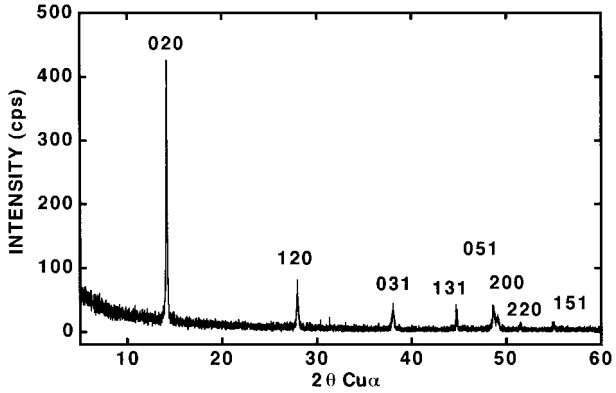

FIGURE 4. XRD pattern of the surface of anorthite after 34 days dissolution at 210 °C. The numbers in the figure represent Miller indices that are based on the boehmite structure. All reflections are attributed to those of modified boehmite.

DISCUSSION

Characterization of modified boehmite

Modified boehmite transforms in the (010) plane to γ-Al_2O_3 by electron irradiation (Fig. 5c) as does boehmite by heating (Brown 1980) or by electron irradiation. The similarity in the transformation and the [010] SAED patterns (Figs. 5a and 5b) indicates that the two-dimensional structure of the Al octahedra of boehmite still exists in modified boehmite. The morphology of boehmite (arrow in Fig. 1a) is similar to that of modified boehmite (arrows in Fig. 1c) except that modified boehmite has a laminated structure (Fig. 1d). The inheritance of the Al octahedral layers and the morphologies suggest that modified boehmite is not formed after boehmite is dissolved, but is formed in and on boehmite. A similar formation mechanism for modified boehmite was also observed in albite and orthoclase dissolution experiments.

Under electron beam irradiation boehmite and modified boehmite are affected differently along the b^* axis, which corresponds to [011] of γ-Al_2O_3. Before damage, boehmite has distinct 0k0 reflections (Fig. 9a) and modified boehmite less distinct reflections (Fig. 6b), but there are no obvious differences in the relative intensities and positions of the 0k0 reflections between the two minerals. After damage, modified boehmite exhibits a diffuse 020 reflection, and weak and very weak diffraction spots at the 040 and 080 positions, respectively, along the b^* axis (Fig. 6c). The γ-Al_2O_3 that formed from boehmite shows weak 022 and strong 044 reflections (Fig. 9b), which correspond to the 040 and 080 reflections of modified boehmite, respectively. These results suggest that modified boehmite cannot be completely transformed to γ-Al_2O_3 by dehydration as boehmite does. A comparison of the microstructure of damaged boehmite (Fig. 9b) strongly indicates that the lattice fringe images of modified boehmite (Figs. 7b and 7c) are not those of damaged boehmite. Modified boehmite contains Al octahedral layers of about 0.6 nm periodicity, normal to the layers, which are identical to those of boehmite. However, modified boehmite loses its periodicity along the b^* axis and shows irregular stacking.

The EQ3NR calculations show that all product solutions were undersaturated with respect to quartz or amorphous silica, and the possibility of the precipitation of nm-sized quartz or amorphous silica on the surface of modified boehmite is unlikely at the experimental temperatures. The absence of quartz or amorphous silica on the surface of grains during the experimental runs or quench was confirmed by our HRTEM and AEM observations of modified boehmite with the electron beam normal to the b^* axis, as shown in Figure 6a. We did not find any microstructures that might indicate the presence of quartz or amorphous silica, or any Si enrichment at the edge. Therefore, the Si contained in modified boehmite is present within its structure and is not due to the

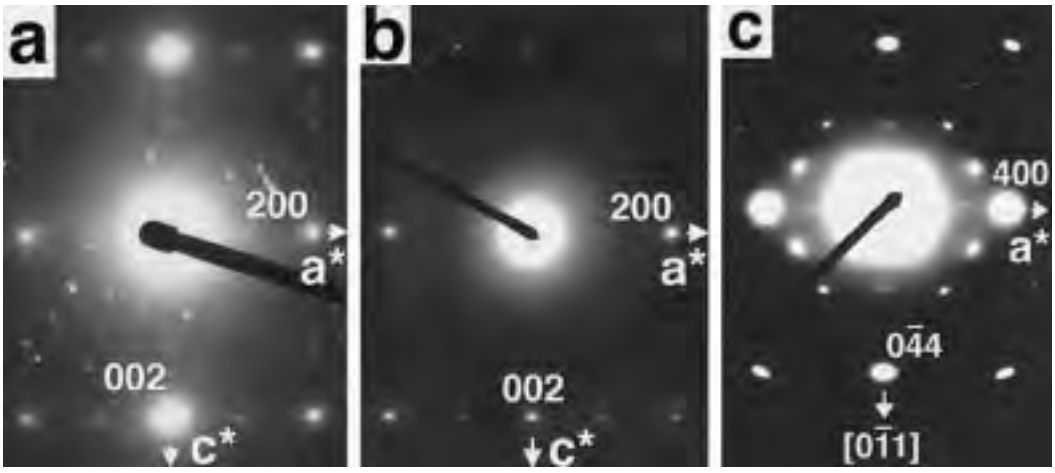

FIGURE 5. [010] SAED patterns of (**a**) modified boehmite, (**b**) boehmite, and (**c**) an [011] SAED pattern of γ-Al_2O_3 formed from modified boehmite after electron irradiation. Extra spots seen in Figure 5a are from adjacent grains.

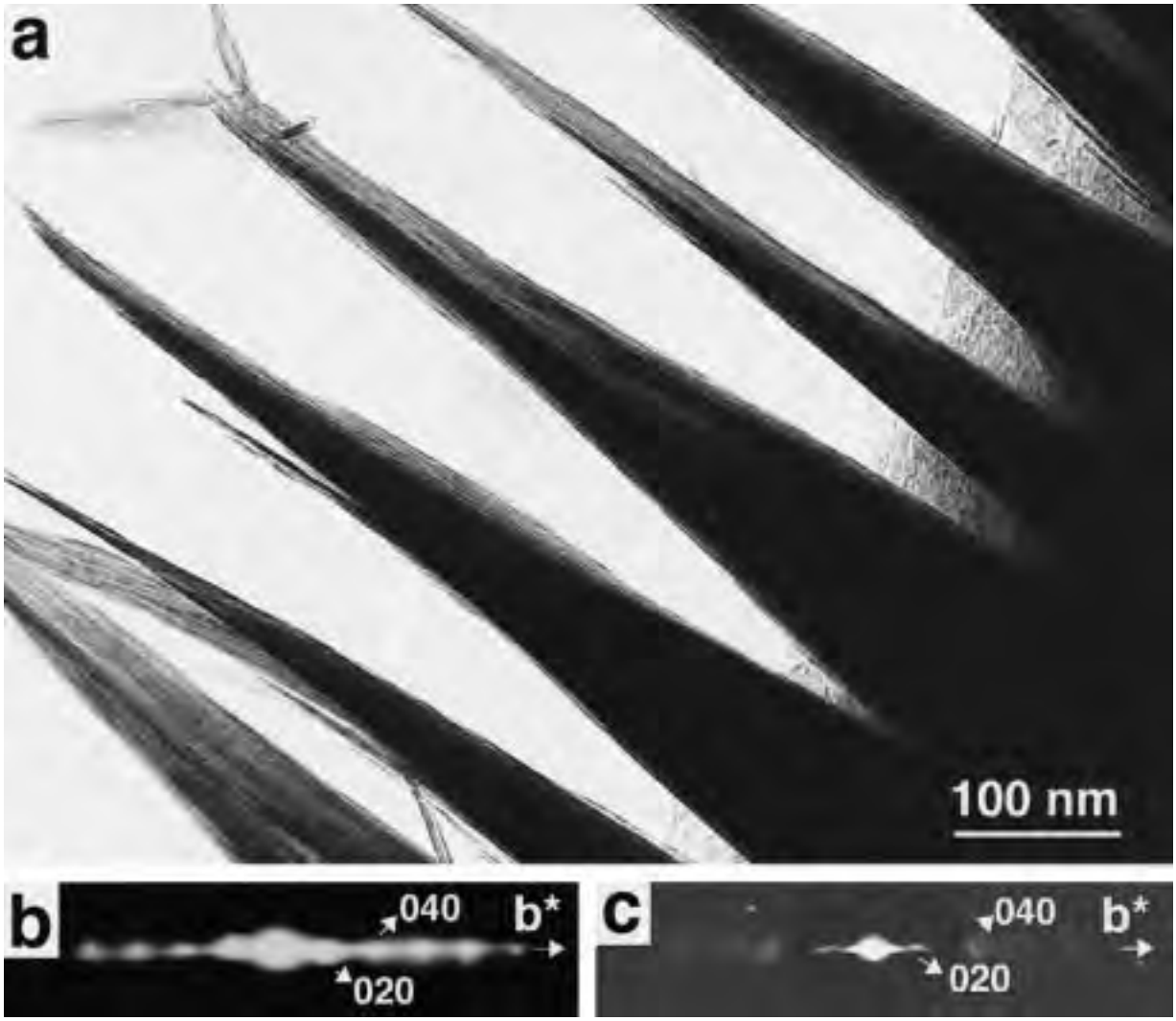

FIGURE 6. TEM image of modified boehmite (**a**), and its SAED patterns (**b**) before and (**c**) after damage. The elongation direction of the laminated structure is approximately normal to *b**.

precipitation of quartz or amorphous silica on the surface of modified boehmite. Although we have not identified the sites of Si cations in the modified boehmite structure, the preservation of the Al octahedral layers and the irregular stacking along the *b** axis suggest Si cations are present between the Al octahedral layers.

Although the XRD pattern of modified boehmite is identical to that of boehmite (Fig. 4), modified boehmite shows irregular stacking along the *b** axis (Figs. 7b and 7c). The SEM-EDX analysis reveals that a grain of modified boehmite contains about 3 mol% Si at the center and about 15 mol% Si at the rim. AEM data show up to 30 mol% Si is contained in the area having the laminated structure such as that shown in Figure 6a. These observations suggest Si is poorer in the core of the grain and richer in the area with the laminated structure. The lattice fringes, as shown in Figure 7a, represent the structure of the core (almost the same as the boehmite structure), whereas the area with the laminated structure (e.g., Fig. 7c) has irregular stacking along the *b** axis. Figures 1d and 6a indicate that the area with the laminated structure extends about 0.7 μm from the core of the grain. However, because of the high porosity of the rims only about half the rim volume consists of crystalline material. Thus, the fraction of the total volume that has a laminated structure is small. This observation explains why the XRD pattern of modified boehmite is almost the same as that of boehmite. Modified boehmite is actually a mixture of an Si-poor part, having almost the same structure as that of boehmite, and an Si-rich part, having a slightly different structure from that of boehmite.

Dissolution affected by the formation of secondary minerals

The dissolution rates of anorthite (moles of anorthite/m^2/s) were calculated based on the Si concentration vari-

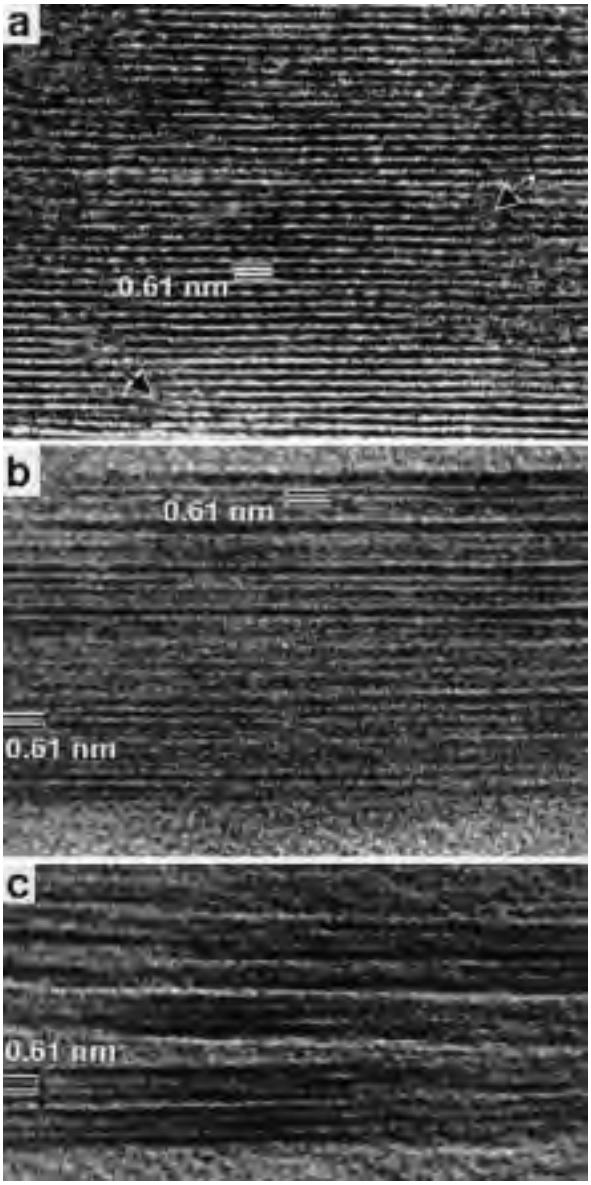

FIGURE 7. HRTEM images of modified boehmite. (**a**) Lattice fringes normal to *b** of a finer-grained modified boehmite. The one-dimensional contrast corresponds to the 0.61 nm periodicity of the Al octahedral layers of boehmite and, thus, the boehmite structure is mostly retained in this grain. Defects such as edge dislocations (e.g., arrows) commonly occur. (**b**) Lattice fringes normal to *b** of another finer-grained modified boehmite. The lattice fringes still show 0.61 nm *d*-spacings but the contrast becomes irregular. (**c**) Lattice fringes normal to *b** of a coarser-grained modified boehmite. The 0.61 nm periodicity is degraded further compared with Figure 7b.

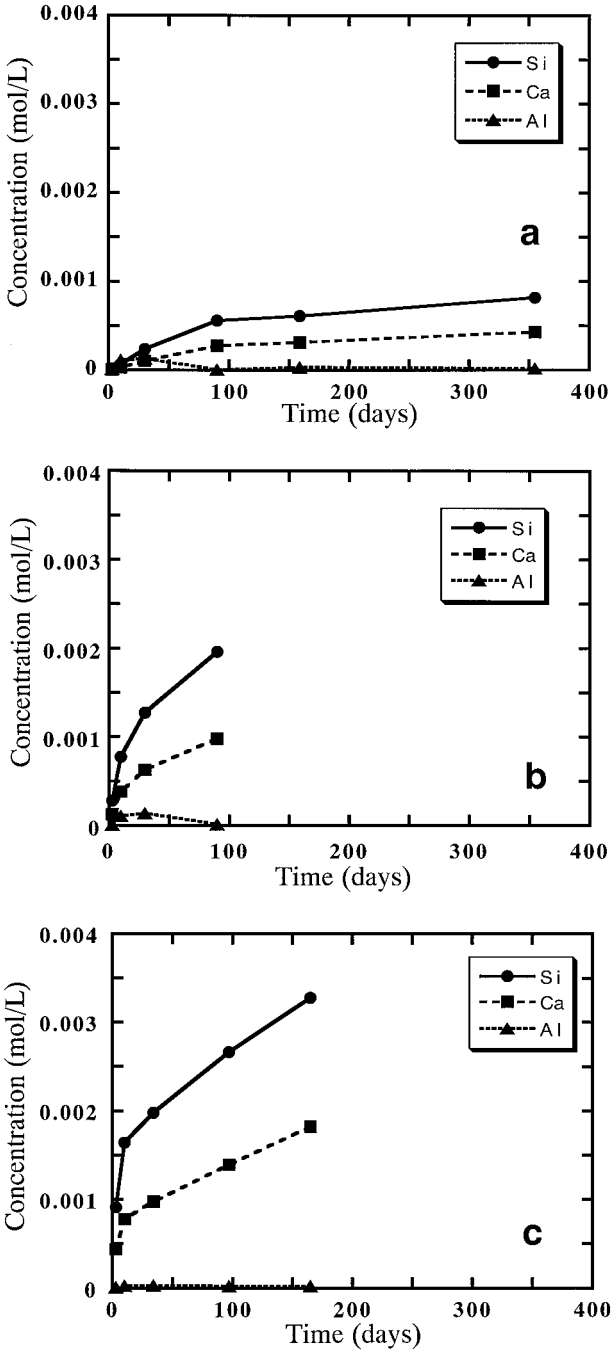

FIGURE 8. Cation concentration variations with time (**a**) for the 90 °C dissolution, (**b**) 150 °C dissolution, and (**c**) 210 °C dissolution.

ation for the first stage, corrected for the Si mole fraction in anorthite (Table 1). For the second stage, the dissolution rates were calculated based on the Ca concentration variation and corrected for the Ca mole fraction in anorthite, because some of the Si released from anorthite is incorporated into modified boehmite and there are no secondary minerals containing Ca. A similar discussion of the nonstoichiometric release of Si and Ca for long-term dissolution has been made by Amrhein and Suarez (1992). The data for the runs at 210 °C for 97 and 165 days were not included in the calculations because kaolinite was formed in these two runs but not in the 90 and 150 °C experiments and, thus, the comparison of the

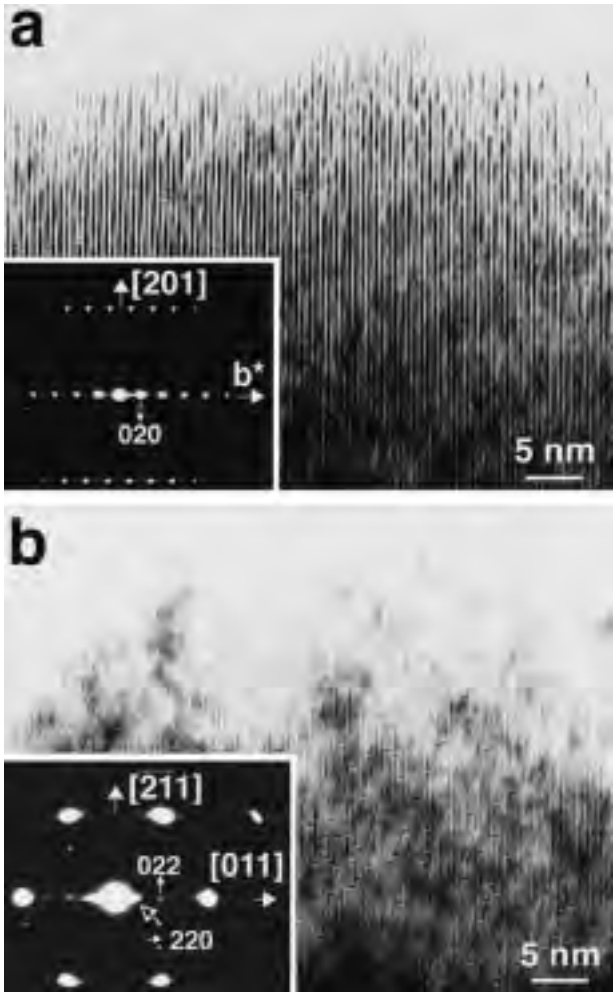

FIGURE 9. Changes in lattice fringe image and diffraction pattern of boehmite before and after electron irradiation damage. (**a**) Lattice fringes of boehmite along the *b** axis that already exhibit a slightly damaged microstructure and (**b**) γ-Al_2O_3 formed from boehmite with respective SAED patterns inset. The lattice fringes in Figure 9b are those of damaged boehmite. An arrow in inset of Figure 9b indicates that the 020 reflection of boehmite still remains.

solution data was difficult. The dissolution rates of anorthite are summarized in Table 3. The dissolution rate in the second stage is slower than the first by approximately one order of magnitude at the temperatures examined, and is even slower (for instance, by 30% based on the 210 °C experiment) when the dissolution rate is calculated based on the Si concentration variation. Modified boehmite is observed to form after the formation of boehmite and before that of kaolinite (Fig. 3). Based on EQ3NR calculations, boehmite forms before quartz or amorphous silica. Thus, with an increase in the activity of SiO_2(aq), modified boehmite is the first secondary mineral that accommodates Si during anorthite dissolution. Modified boehmite functions as a sink for Si in the second stage, which affects the distribution of Si between solid and solution.

TABLE 3. Dissolution rates (moles of anorthite/m²/s)

	90 °C	150 °C	210 °C
The first stage	1.41×10^{-8}	1.20×10^{-7}	1.70×10^{-7}
The second stage	1.52×10^{-9}	1.38×10^{-8}	2.03×10^{-8}

Note: Based on Si and Ca released during the first and second stages, respectively.

The dissolution rate should depend on (Q/K) or the Gibbs free energy when the dissolution is congruent and the secondary phase is the same as the primary phase (Lasaga 1984). In the present study, anorthite dissolution is incongruent because of the formation of secondary minerals that are compositionally different from anorthite. However, a comparison of Gibbs free energy with dissolution rates is useful for examining which factors affect the dissolution. The dissolution rate for each run (Table 3) was plotted against the Gibbs free energy of anorthite dissolution, ΔG, where $\Delta G = RT \ln (Q/K)$ (R is the gas constant and T is the temperature). Values of ln (Q/K) at the experimental temperatures were calculated using EQ3NR. Figure 10 (solid symbols) shows the relationships between the dissolution rates of anorthite and ΔG, which indicates that the dissolution rates are affected by the saturation state of anorthite, as in the case of albite and potassium feldspar dissolution (Burch et al. 1993; Gautier et al. 1994; Oelkers et al. 1994).

In the next step, we assumed there was no precipitation of boehmite or modified boehmite, and the dissolution was congruent. The Si, Al, and Ca concentrations in solution in the two stages were calculated based on the measured Si and Ca concentrations (Table 2) in the first and second stages, respectively. ΔG_{cor} values at the experimental temperatures were then calculated, corrected for congruent dissolution after the calculation of Q_{cor}/K by EQ3NR, where ΔG_{cor} and Q_{cor} are the Gibbs free energy of anorthite dissolution and activity product after correction, respectively. The dissolution rates in Table 3 were plotted against ΔG_{cor}. The ΔG_{cor} values are shifted to larger values (open symbols in Fig. 10), indicating that the formation of the secondary minerals decreases the ΔG values of the dissolution (arrows in the inset of Fig. 10). By decreasing ΔG, the dissolution rate of anorthite increases (e.g., Lasaga 1984). We can predict that the dissolution rates of anorthite increase due to the influence of the secondary minerals on ΔG. Indeed, some of the solutions are supersaturated with respect to anorthite without the formation of the secondary minerals (open symbols in Fig. 10).

The relation of the dissolution rates to ΔG and ΔG_{cor} reveals that the saturation with respect to anorthite decreases the dissolution rate near equilibrium on the one hand, and the formation of secondary minerals increases the rate on the other hand. The overall dissolution rate is controlled by the saturation and secondary mineral for-

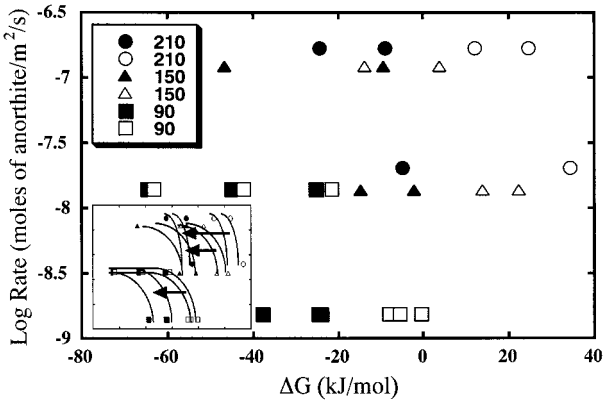

FIGURE 10. Relationships between the dissolution rates and Gibbs free energies of anorthite dissolution, ΔG, at the experimental temperatures. Squares = 90 °C; triangles = 150 °C; and circles = 210 °C. The solid symbols correspond to ΔG values calculated based on the measured cation concentrations, and the open symbols to those calculated assuming congruent dissolution without the formation of secondary minerals (see text for further explanation). The arrows in the inset illustrate a decrease in ΔG values brought about by the formation of secondary minerals.

mation, but in the opposite sense. The saturation has a larger effect on the dissolution rate than secondary phase formation near equilibrium ($\Delta G \gtrsim -30$ kJ/mol), which results in the slower rate at the second stage (Fig. 8). The dissolution rate is even slower without the formation of secondary minerals, where the saturation alone influences the rate. In addition, the results of our calculation strongly suggest that the amount of secondary minerals affects the dissolution rate because of the relation of their amount to the activity product, and thus to the Gibbs free energy. By lowering apparent ΔG, the formation of secondary minerals retards the attainment of equilibrium with respect to the primary phase, which provides further confirmation that the paragenesis of secondary minerals affects elemental distribution and transport.

Although Velbel (1989) concluded a saturation state effect is negligible and cannot explain the discrepancy between field and experimental feldspar dissolution rates, Amrhein and Suarez (1992) demonstrated that the final reaction rate after long-term dissolution of anorthite (up to 4.5 years) is slower by a few orders of magnitude due to the effect of saturation. The present experimental environments are similar to those in nature where secondary minerals are found within and between grains of primary phases. In such environments, even though the formation of secondary minerals may increase the dissolution rate, the overall dissolution rate significantly decreases due to the saturation effect. This finding partly explains the discrepancy of dissolution or weathering rates between laboratory and field observations.

ACKNOWLEDGMENTS

The authors are indebted to T. Banba and Y. Tamura at the Japan Atomic Energy Research Institute (JAERI) for the analyses of solutions, to N. Yanagisawa of the Geological Survey of Japan for the SEM-EDX analysis, and to K. Shimizu at the Museum of the University of Tokyo for the SEM examination. The authors also thank H. Isobe and T. Sato at JAERI for valuable discussions, and T. Tachikawa for the technical assistance. J.F. Banfield is acknowledged for her comments on an earlier version of the manuscript. The authors thank the reviewers, A.J. Brearley, L.L. Stillings, and D.R. Veblen for their helpful comments. Part of the electron microscopy was performed in the Electron Microbeam Analysis Facility of the Mineralogical Institute, the University of Tokyo. Part of the present study was supported by a Scientific Grant of the Ministry of Education, Science and Culture (Nos. 6640620 and 9440184).

REFERENCES CITED

Alekseyev, V.A., Medvedeva, L.S., Prisyagina, N.I., Meshalkin, S.S., and Balabin, A.I. (1997) Change in the dissolution rates of alkali feldspars as a result of secondary mineral precipitation and approach to equilibrium. Geochimica et Cosmochimica Acta, 61, 1125–1142.

Amrhein, C. and Suarez, D.L. (1992) Some factors affecting the dissolution kinetics of anorthite at 25 °C. Geochimica et Cosmochimica Acta, 56, 1815–1826.

Banfield, J.F. and Eggleton, R.A. (1990) Analytical transmission electron microscope studies of plagioclase, muscovite, and K-feldspar weathering. Clays and Clay Minerals, 38, 77–89.

Banfield, J.F., Jones, B.F., and Veblen, D.R. (1991) An AEM-TEM study of weathering and diagenesis, Albert Lake, Oregon (1) Weathering reaction in the volcanics. Geochimica et Cosmochimica Acta, 55, 2781–2793.

Banfield, J.F., Veblen, D.R., and Jones, B.F. (1990) Transmission electron microscopy subsolidus oxidation and weathering of olivine. Contribution to Mineralogy and Petrology, 106, 110–123.

Bence, A.E. and Albee, A.L. (1968) Empirical correction factors for the electron microanalysis of silicates and oxides. Journal of Geology, 76, 382–403.

Berner, R.A. (1992) Weathering, plants and the long-term carbon cycle. Geochimica et Cosmochimica Acta, 56, 3225–3231.

———(1995) Chemical weathering and its effect on atmospheric CO_2 and climate. In Mineralogical Society of America Reviews in Mineralogy, 31, 565–583.

Berner, R.A. and Barron, E.J. (1984) Comments on the BLAG model: Factors affecting atmospheric CO_2 and temperature over the past 100 million years. American Journal of Science, 284, 1183–1192.

Berner, R.A., Lasaga, A.C., and Garrels, R.M. (1983) The carbonate-silicate geochemical cycle and its effect on atmospheric carbon dioxide over the past 100 million years. American Journal of Science, 283, 641–683.

Blatt, H. and Jones, R.L. (1975) Proportions of exposed igneous, metamorphic, and sedimentary rocks. Geological Society of America Bulletin, 86, 1085–1088.

Blum, A.E. and Stillings, L.L. (1995) Feldspar dissolution kinetics. In Mineralogical Society of America Reviews in Mineralogy, 31, 291–351.

Blum, A.E. (1994) Feldspars in weathering. In I. Parsons, Ed., Feldspars and their reactions, p. 595–629. Kluwer Academic Publications, The Netherlands.

Brady, P.V. (1991) The effects of silicate weathering on global temperature and atmospheric CO_2. Journal of Geophysical Research, 96(B11), 18101–18106.

Brady, P.V. and Caroll, S.A. (1994) Direct effects of CO_2 and temperature on silicate weathering: possible implications for climate control. Journal of Geophysical Research, 58, 1853–1856.

Brown, G. (1980) Associated minerals. In G.W. Brindley and G. Brown, Eds., Crystal Structures of Clay Minerals and Their X-ray Identification, p. 361–410. Mineralogical Society, London.

Burch, T.E., Nagy, K.L., and Lasaga, A.C. (1993) Free energy dependence of albite dissolution kinetics at 80 °C and pH 8.8. Chemical Geology, 105, 137–162.

Casey, W.H., Banfield, J.F., Westrich, H.R., and McLaughlin, L. (1993a) What do dissolution experiments tell us about natural weathering? Chemical Geology, 105, 1–15.

Casey, W.H., Westrich, H.R., Banfield, J.F., Ferruzzi, G., and Arnolds,

G.W. (1993b) Leaching and reconstruction at the surfaces of dissolving chain-silicate minerals. Nature, 366, 253–256.

Christoph, G.G., Corbató, C.E., Hofmann, D.A., and Tettenhorst, R.T. (1979) The crystal structure of boehmite. Clays and Clay Minerals, 27, 81–86.

Franklin, S.P., Hajash, A., Dewers, TA., and Tieh, T.T. (1994) The role of carboxylic acids in albite and quartz dissolution: An experimental study under diagenetic conditions. Geochimica et Cosmochimica Acta, 58, 4259–4279.

Gautier, J.M., Oelkers, E.H., and Schott, J. (1994) Experimental study of K-feldspar dissolution rates as a function of chemical affinity at 150 °C and pH 9. Geochimica et Cosmochimica Acta, 58, 4549–4560.

Harada, J. and Hariya, Y. (1984) Minerals in Hokkaido, 327 p. Underground Resource Survey of Hokkaido, Hokkaido, Japan (in Japanese).

Hellmann, R. (1994) The albite-water system: Part I. The kinetics of dissolution as a function of pH at 100, 200, and 300 °C. Geochimica et Cosmochimica Acta, 58, 595–611.

Hochella, M.F. Jr. and Banfield, J.F. (1995) Chemical weathering of silicates in nature: A microscopic perspective with theoretical considerations. In Mineralogical Society of America Reviews in Mineralogy, 31, 353–406.

Lasaga, A.C. (1984) Chemical kinetics of water-rock interactions. Journal of Geophysical Research, 89, 4009–4025.

Lasaga, A.C., Soler, J.M., Ganor, J., Burch, T.E., and Nagy, K.L. (1994) Chemical weathering rate laws and global geochemical cycles. Geochimica et Cosmochimica Acta, 58, 2361–2386.

Nagy, K.L. (1995) Dissolution and precipitation kinetics of sheet silicates. In Mineralogical Society of America Reviews in Mineralogy, 31, 173–233.

Oelkers, E.H., Schott, J., and Devidal, J.-L. (1994) The effect of aluminum, pH, and chemical affinity on the rates of aluminosilicate dissolution reactions. Geochimica et Cosmochimica Acta, 58, 2011–2024.

Rooksby, H.P. (1961) Oxides and hydroxides of iron and aluminum. In G.W. Brindley and G. Brown, Eds., Crystal Structures of Clay Minerals and Their X-ray Identification, p. 361–410. Mineralogical Society, London.

Rowe, G.L. Jr. and Brantley, S.L. (1993) Estimation of the dissolution rates of andesitic glass, plagioclase and pyroxene in a flank aquifer of Poás Volcano, Costa Rica. Chemical Geology, 105, 71–87.

Schnoor, J.L. (1990) Kinetics of chemical weathering: A comparison of laboratory and field weathering rates. In W. Stumm, Ed., Aquatic chemical kinetics: Reaction rates of processes in natural waters, p. 475–505. Wiley, New York.

Swoboda-Colberg, N.G. and Drever, J.I. (1993) Mineral dissolution rates in plot-scale field and laboratory experiments. Chemical Geology, 105, 51–69.

Velbel, M.A. (1989) Effect of chemical affinity on feldspar hydrolysis rates on two natural weathering systems. In J. Schott and A.C. Lasaga, Eds., Kinetic Geochemistry. Chemical Geology, 78, 245–253 (special issue).

———(1990) Influence of temperature and mineral surface characteristics on feldspar weathering rates on natural and artificial systems. Water Resources Research, 26, 3049–3053.

———(1993) Constancy of silicate mineral weathering-rate ratios between natural and experimental weathering—Implications for hydrologic control of differences in absolute rates. Chemical Geology, 105, 89–99.

Velde, B. and Meunier, A. (1987) Petrologic phase equilibria in natural clay systems. In A.C.D. Newman, Ed., Chemistry of clays and clay minerals, p. 423–458. Mineralogical Society, London.

Welch, S.A. and Ullman, W.J. (1993) The effect of organic acids on plagioclase dissolution rates and stoichiometry. Geochimica et Cosmochimica Acta, 57, 2725–2736.

White, A.F. and Brantley, S.L., Eds. (1995) Chemical weathering rates of silicate minerals. In Mineralogical Society of America Reviews in Mineralogy, vol. 31.

Wolery, T.J. (1992) EQ3NR, A computer program for geochemical aqueous speciation-solubility calculations: Theoretical manual, user's guide, and related documentation (version 7.0), UCRL-MA-110662 PT III, 246 p. Lawrence Livermore Laboratory, University of California.

Manuscript received September 5, 1997
Manuscript accepted July 14, 1998
Paper handled by Adrian J. Brearley